Journal of
Composites Science

MDPI

Article

Thermal Ageing of a Hybrid Composite Rod for Next Generation Overhead Power Lines

Gaelle Minard and Xavier Colin *

Laboratoire PIMM (UMR CNRS 8006), ARTS ET METIERS, 151 Boulevard de l'Hôpital, 75013 Paris, France; gaelle.minard@ensam.eu

* Correspondence: xavier.colin@ensam.eu; Tel.: +33-1-44-24-61-47

Received: 1 November 2019; Accepted: 22 November 2019; Published: 27 November 2019

Abstract: The thermal stability of a hybrid composite rod, made of epoxy-anhydride matrix reinforced with both unidirectional carbon and glass fibers, has been evaluated between 180 and 210 °C in different nitrogen/oxygen gas mixtures with several conventional but complementary laboratory techniques such as Fourier transform infrared spectrometry, thermogravimetry, differential calorimetry, optical microscopy, and three-point bending. Thermolysis predominates in the carbon-fiber core, where it induces an efficient chain scission process, leading to a decrease in the glass transition temperature and the formation of small macromolecular fragments, presumably diacids. These very polar fragments remain trapped in the carbon core, where they initiate micro-cavities when their concentration exceeds the solubility threshold. These micro-cavities accumulate in rich-matrix regions, where they coalesce to form apparent large cracks. They are thus responsible for the catastrophic decrease in elastic and fracture properties of the composite rod. In contrast, thermal oxidation affects a too thin superficial layer (typically 60 μm) of the glass-fiber shell to change significantly the global mechanical behavior of the composite rod. Based on these experimental observations, a kinetic model has been proposed to predict the initiation and development of damage in the composite rod. Its validity is successfully checked by comparing its predictions with the experimental results.

Keywords: hybrid composite; anhydride crosslinked epoxy; thermal ageing; chain scissions; micro-cavities; embrittlement

1. Introduction

The request for electricity increases constantly over the world. Faced with environmental and societal pressures opposed to the construction of new overhead power lines, electricity distributors need new technical solutions for increasing the nominal rating of the present lines. The average operating temperature of these is around 70 °C, but it could be increased beyond 90 °C in a near future. Several technical solutions are under study to avoid a catastrophic increase in the sag, but they will be selected by electricity distributors only if the long-term thermal stability of their different constituent materials is well demonstrated.

The aim of the present study is to evaluate the feasibility of a new conductor technology especially designed for the next generation overhead lines. It consists of an aluminum conductor supported by a hybrid composite core made of epoxy matrix reinforced with both unidirectional carbon and glass fibers (Figure 1). Carbon fibers have been selected for this application because of the very low value of their thermal expansion coefficient in the longitudinal direction [1], thus allowing to design lines with a sag almost independent of temperature variations. However, carbon fibers have been replaced by glass fibers within the composite shell to avoid the galvanic corrosion of the surrounding aluminum conductor [2].

Figure 1. Aluminum conductor supported by a hybrid composite core.

Unfortunately, the durability of this hybrid composite rod has been the subject of very few research works to date [3–5]. At high temperature (typically 180 and 200 °C) in air, it has been shown that the outer superficial layer of the glass-fiber shell is subjected to a thermal oxidation leading to both mass loss and densification of the epoxy matrix. The resulting "hindered" shrinkage induces the development of a gradient of tensile stresses in the oxidized layer that is responsible, at more or less long term, for its spontaneous cracking. It should be emphasized that these stresses are amplified by the increase in the Young's modulus during the course of oxidation [3,5]. However, the incorporation of mineral fillers (in particular, kaolinite clays) into the formulation of the epoxy matrix has no impact on its oxidation kinetics and, thus, on the damage development in the composite rod [5].

Despite the high quality of these researches, some crucial questions remain unanswered. In particular, it would be surprising that the degradation of such a thin superficial layer (typically 110–120 μm at 200 °C, which represents only 2–3% of the rod radius) allows explaining alone the dramatic decrease in shear strength of the composite material [5]. However, the same authors also report a significant mass loss in the absence of oxygen (typically 10 wt% after 200 h at 200 °C in inert atmosphere or under vacuum) that they do not discuss and interpret [3,5]. Could it be a thermolysis of the epoxy matrix? Could this additional degradation process affect the entire volume of the composite rod and, thus, explain still non-understood changes in its mechanical behavior in the long term.

The present study focuses on the understanding of the thermal ageing of the composite rod at high temperature (typically between 180 and 210 °C) in different nitrogen/oxygen gas mixtures. A multi-scale analysis involving several conventional but complementary laboratory techniques will be applied to try to identify the different degradation mechanisms of the epoxy matrix. Then, a kinetic model will be derived from these mechanisms to predict the initiation and development of damage in the composite material. The validity of several assumptions necessary for building this model will have to be checked in future research works.

2. Materials and Methods

The composite rod under study consists in a carbon-fiber core (outer diameter = 7.0 mm, volume fraction of fibers = 69%) surrounded by a glass-fiber shell (outer diameter = 9.5 mm, volume fraction of fibers = 64%). It was processed by pultrusion at 200 °C by the Merwyn C. Gill Foundation Composites Center. The composite matrix results from the reaction of several epoxy monomers with an anhydride hardener. It is filled by about 12 wt% of kaolinite clays.

This hybrid composite material is relatively easy to machine. Samples of various geometric shapes (cylindrical or rectangular bars, powder, etc.) were taken in different parts of the rod, thus offering the possibility of studying separately the different constituent materials. As an example, the glass-fiber shell was totally removed from the rod to be separately characterized from the carbon-fiber core before and after thermal ageing. In addition, steps of about 0.5 mm in height were machined in the diameter of the carbon-fiber core (Figure 2) and a small amount of powder was then taken at the surface of

each step in order to determine the gradients of chemical structure and physicochemical properties throughout the rod diameter before and after thermal ageing.

Figure 2. Carbon-fiber core after glass-fiber shell removing and steps machining.

The different shapes of samples used for the present study (with their corresponding size) are listed in Table 1.

Table 1. Samples under study.

Material	Shape	Size (mm)
hybrid composite	cylindrical bar	9.5 × 100
carbon-fiber core	cylindrical bar	7.0 × 70
-	rectangular bar	1.2 × 4.2 × 30
-	powder	-
glass-fiber shell	powder	-

On the one hand, hybrid composite rods were thermally aged between 180 and 210 °C in nitrogen or ambient air in ovens. They were removed periodically from the ovens to be analyzed with several conventional laboratory techniques. Some rods were characterized by three-point bending tests (Instron 4502 device, distance between supports of 80 mm, crosshead speed of 2 mm·s^{-1}) according to the recommendations of the standard NF EN ISO 178 [6]. These tests were carried at the current operating temperature of the overhead power lines, i.e., 70 °C. A peculiar attention was paid to the changes in the breaking stress and flexural modulus.

Some other rods were examined by optical microscopy after cutting in small pieces, embedding in a commercial acrylic KM-V resin, and polishing of their cross sections with a MECAPOL P320 device (Grenoble, France) using silicon carbide abrasive papers of decreasing particle size (typically from 80 to 4000 granulometry). Then, a mirror finish was obtained using diamond pastes of decreasing particle size (typically from 3 to 0.25 μm).

Finally, the last rods were analyzed by FTIR spectrometry (Brüker IFS 28 device, Ettlingen, Germany, 4 cm^{-1} minimal resolution) and differential calorimetry (TA Instrument Q10 DSC, New Castle, DE, USA, heating rate of 20 °C·min^{-1}, nitrogen flow of 50 mL·min^{-1}) after steps machining (Figure 2). Powder samples of about 15–20 mg were taken from the surface of each step for monitoring the changes in the molecular and macromolecular structures of the epoxy-anhydride matrix, respectively. In some cases only, a rectangular bar was also machined in the center of the carbon-fiber core to be analyzed by viscoelasticimetry (Rheometrics RDA3 torsiometer, New Castle, DE, USA, heating rate of 5 °C·min^{-1}, frequency of 1 Hz, nitrogen flow) and, thus, to confirm the corresponding value of the glass transition temperature (T_g) measured by differential calorimetry (DSC).

On the other hand, powder samples of about 15–20 mg of each constituent material (i.e., carbon-fiber core and glass-fiber shell) were aged thermally at 180, 190, 200, and 210 °C in various nitrogen/oxygen gas mixtures directly in the furnace of a thermogravimeter (Netzsch Tg 209 device, Netzsch Gerätebau, Germany, nitrogen flow of 50 mL·min^{-1}). The samples were directly placed on the plateau of the microbalance, and their mass changes were continuously recorded versus time of exposure in a computer.

3. Experimental Results

Experimental results are summarized in the following sections.

3.1. Mechanical Characterization

Figure 3 shows an example of a load-displacement curve obtained for the virgin composite rod. This bending behavior can be qualified as brittle since it consists almost exclusively of an elastic domain marked above half of the maximum load by the presence of sudden small drops of load due to cracks initiation in the central region of the carbon-fiber core. It should be emphasized that this central region may contain many processing defects (such as porosities, micro-cracks, etc.), which can explain its lower mechanical strength. In addition, during the bending test, this central region is subjected to high shear stresses.

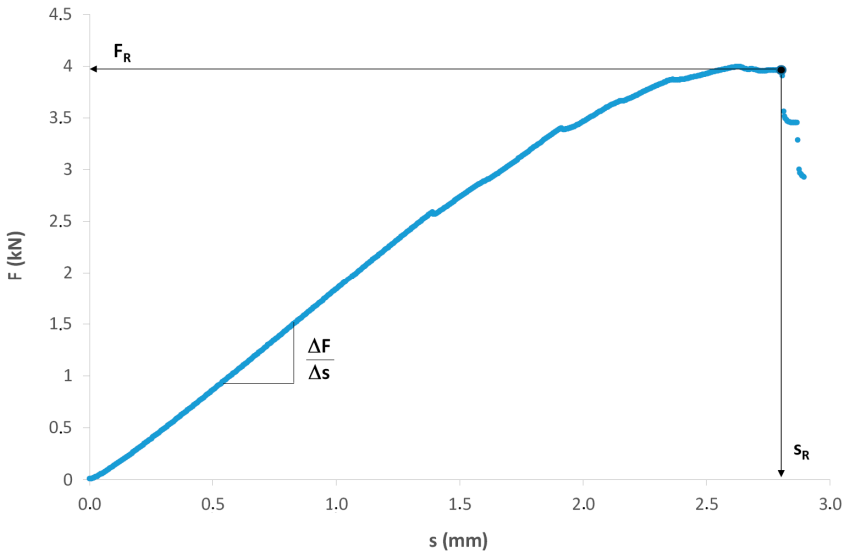

Figure 3. Example of load-displacement curve for the virgin composite rod.

The elastic domain ends with a very short plateau during which the cracks propagate rapidly in the perpendicular direction of the load, i.e., in the longitudinal direction of the composite rod. Finally, when it breaks, the rod separates into two equivalent parts.

Three important characteristics were determined graphically from the load-displacement curve of Figure 3: The maximal slope of the elastic regime ($\Delta F/\Delta s$), the breaking load (F_R), and the breaking sag (s_R). The values of the bending modulus E and the breaking stress σ_R were calculated by applying the following classical formulas:

$$E = \frac{4L^3}{3\pi D^4}\frac{\Delta F}{\Delta s} \quad (1)$$

$$\sigma_R = \frac{8F_R L}{\pi D^3} \quad (2)$$

where L is the distance between supports (L = 80 mm) and D is the rod diameter (D = 9.5 mm). The bending properties of the virgin composite rod are summarized in Table 2.

Table 2. Bending properties of the virgin composite rod.

E (GPa)	σ_R (MPa)	s_R (mm)
48.9 ± 0.6	838 ± 50	2.46 ± 0.20

The thermal ageing of the composite rod between 180 and 210 °C in nitrogen or ambient air leads to a drop in E and σ_R from the early periods of exposure, as shown in Figure 4. However, this drop is less marked for E than for σ_R. As an example, E decreases by about 4% after 25 h at 210 °C or 300 h at 180 °C, while σ_R decreases by about twice (i.e., 8%). In addition, the drop in E is strongly slowed

down, while it remains almost linear for σ_R. The damage causing this peculiar mechanical behavior will be examined in the following section.

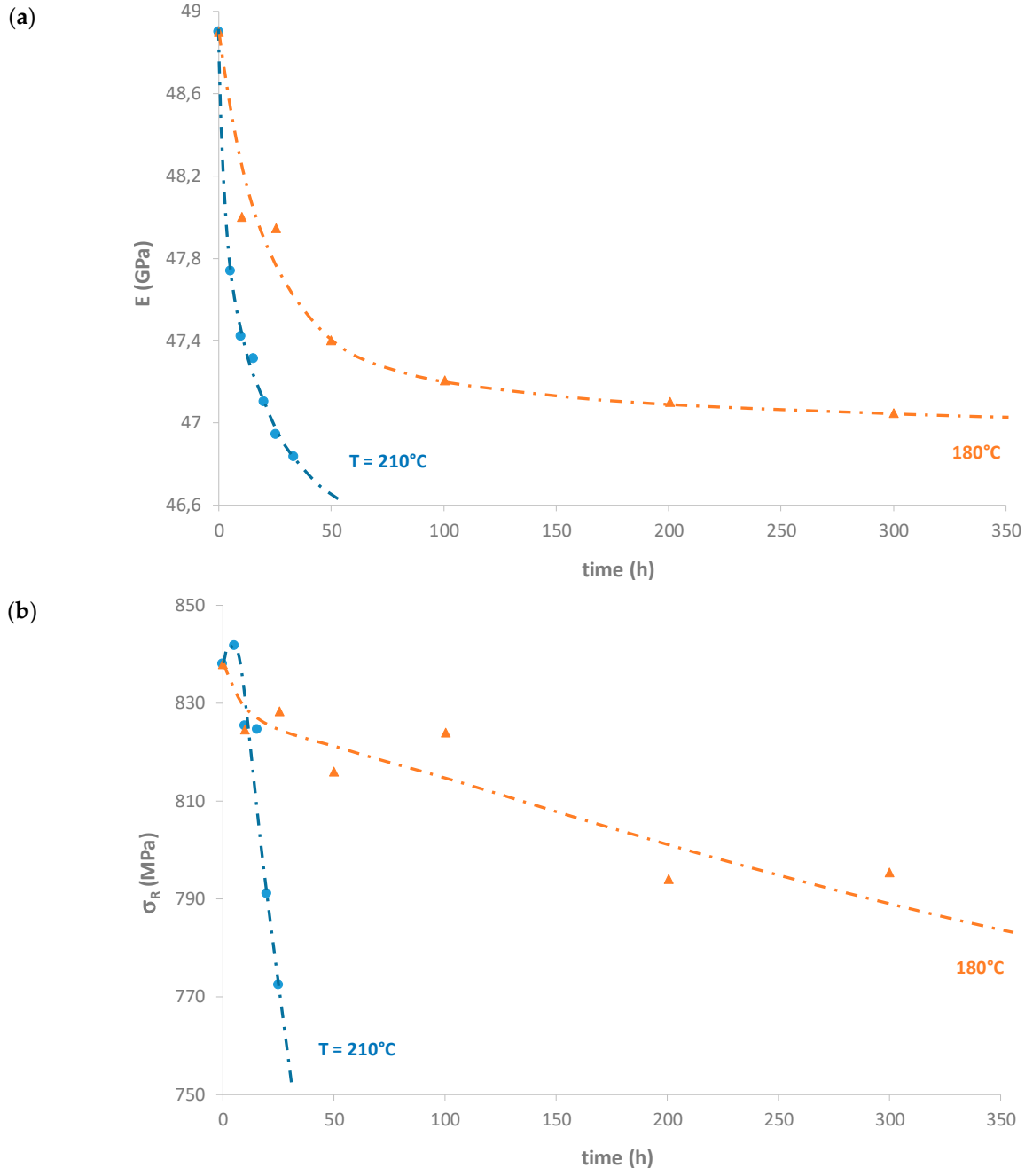

Figure 4. Changes in the bending behavior of the composite rod during its thermal ageing at 180 and 210 °C in nitrogen or ambient air: (**a**) bending modulus and (**b**) breaking stress.

3.2. Optical Microscopic Examinations

First of all, Figure 5 reports examples of micrographs of the radial cross section of the as-received composite rod. These micrographs were taken at random in the interfacial region between the carbon-fiber core and the glass-fiber shell at three different magnifications (×5, ×10, and ×20). It can be clearly seen that the interface separating both materials is not perfectly circular but very sinuous due to the deposition of pre-impregnated glass-fiber wicks over the carbon-fiber core during the pultrusion

process. In the two constituent materials, fibers appear to be fairly homogeneously distributed, although some small rich-matrix regions can be observed here and there.

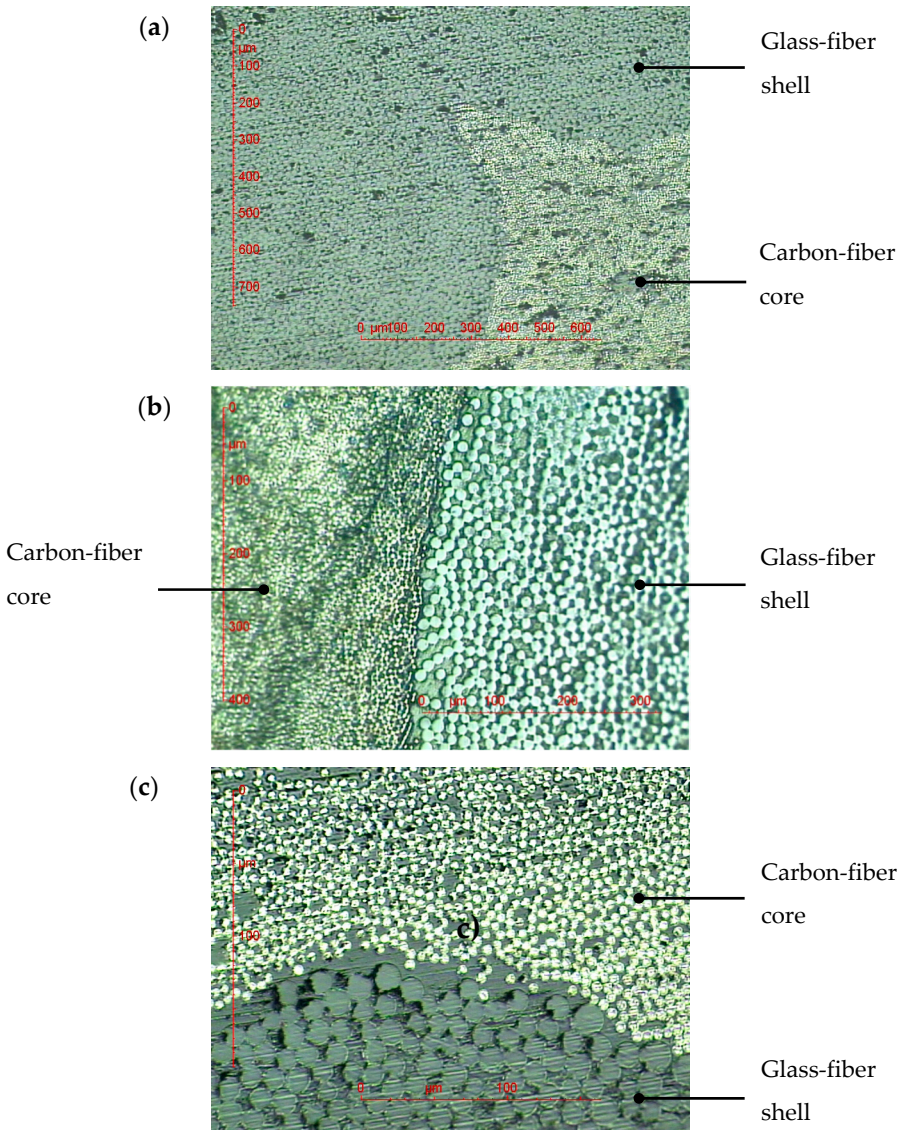

Figure 5. Examination by optical microscopy of the radial cross section of the as-received composite rod: Magnifications are (**a**) ×5, (**b**) ×10, and (**c**) ×20.

The average diameter of the fibers and their volume fraction were determined by image analysis with the ImageJ software. They are about 5 µm and 70 vol% for carbon fibers and 15 µm and 65 vol% for glass fibers. These values are quite consistent with the announcements of the composite manufacturer.

It should be noted that a small population of the as-received composite rods already contained some cracks of circular shape all around the central carbon-fiber wick (see Figure 6). These cracks were presumably created by too fast cooling of the rods at the exit of the pultrusion line. Of course, these defective rods were excluded from the present study.

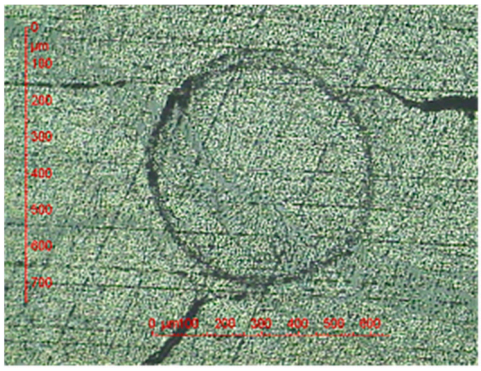

Figure 6. Examination by optical microscopy of the carbon-fiber core of the as-received composite rod: Evidence of cracks around the central carbon-fiber wick. Magnification is ×5.

Then, Figure 7 reports an example of micrographs of the radial cross section of composite rods thermally aged in nitrogen or ambient air in ovens. These micrographs were taken in the carbon-fiber core at low magnification (×5).

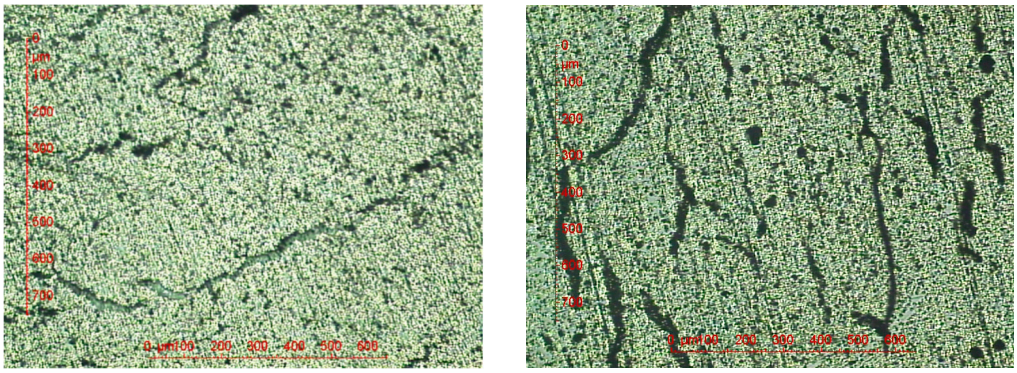

(**a**) (**b**)

Figure 7. Examination by optical microscopy of the carbon-fiber core of the composite rod: (**a**) after 100 h in nitrogen at 190 °C and (**b**) after 90 h in ambient air at 200 °C. In both cases, magnification is ×5.

Between 180 and 210 °C, thermal ageing leads to the formation of many large cracks in the carbon-fiber core, irrespective of the nature of the exposure atmosphere. A careful examination at higher magnification reveals that these cracks have been, in fact, formed in rich-matrix regions and are constituted of many micro-cavities juxtaposed against each other, like a pearl necklace. No doubt, these large cracks result from the coalescence of micro-cavities. In addition, since they are formed in the total absence of oxygen, it can be concluded that they can only result from the thermolysis of the epoxy-anhydride matrix.

Finally, Figure 8 reports an example of micrographs of the radial and longitudinal cross section of a composite rod thermally aged in ambient air in oven. These micrographs were taken in the free edge of the glass-fiber shell at low magnification (×5).

Between 180 and 210 °C, thermal ageing in ambient air leads to the formation of a superficial oxidized layer in the free edge of the glass-fiber shell, of which the thickness depends closely on the ageing temperature and fiber orientation, as already observed for other types of unidirectional composite material, in particular made of epoxy-diamine matrix [7]. The oxidized layer appears as a darker area than the unaffected parts of the glass-fiber shell. For a better visualization, this layer was delimited with yellow dotted lines on micrographs.

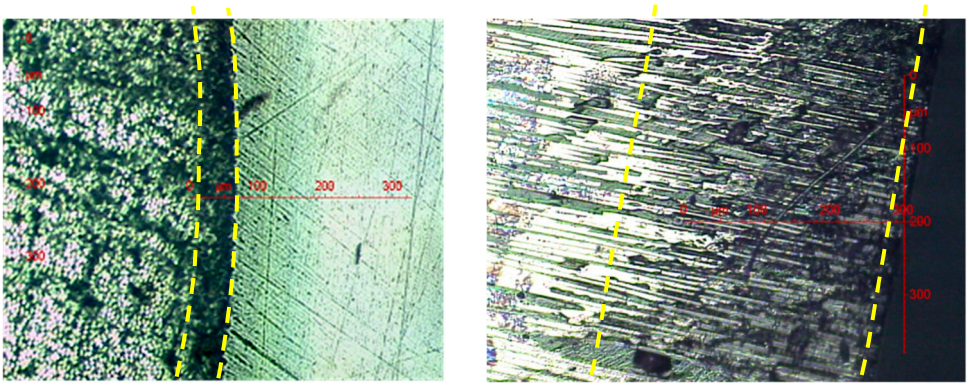

(**a**) (**b**)

Figure 8. Examination by optical microscopy of the free edge of the glass-fiber shell of the composite rod after 100 h in ambient air at 180 °C: (**a**) in the radial direction and (**b**) in the longitudinal direction. In both cases, magnification is ×5.

In both (radial and longitudinal) directions of the composite rod, the thickness of the superficial oxidized layer (TOL) increases with time of exposure until reaching an asymptotic value, which is reported in Table 3.

Table 3. Maximal values of the superficial oxidized layer (TOL) in the different directions of the composite rod in ambient air at 180 and 210 °C.

Material	Direction	Temperature (°C)	TOL (µm)
glass-fiber shell	radial	180	60
-	-	210	60
-	longitudinal	180	450
-	-	210	230

As expected [7], TOL is much larger in the longitudinal direction where oxygen diffusion is favored (no fiber obstacle) than in the radial direction where diffusion paths are much longer. In a first approach, the model of Kondo et al. [8] based on simple geometric considerations can be used to illustrate this problem. According to these authors, the diffusivities in the perpendicular ($D_{\perp}$) and parallel directions to the fibers ($D_{//}$) would be related by the following relationship:

$$D_{\perp} = \frac{1 - \alpha\sqrt{V_f}}{1 - V_f} D_{//} \tag{3}$$

where V_f is the volume fraction of fibers and α is a constant such as $\alpha = 2/\sqrt{\pi}$ for a cubic stack and $\alpha = \sqrt{2\sqrt{3}/\pi}$ for a hexagonal stack of fibers [9].

In addition, the diffusivity in the parallel direction is given by the following [10]:

$$D_{//} = \left(1 - V_f\right) D_m \tag{4}$$

where D_m corresponds to the coefficient of oxygen diffusion in the neat matrix. The introduction of the volume fraction of glass fibers (V_f = 64 vol%) in Equations (3) and (4) leads finally to $D_{//} = 3.7 \times D_{\perp}$ and $D_m = 2.8 \times D_{//}$ for a cubic stack.

At this stage of investigations, let us remember that TOL can be satisfyingly predicted by a simple scale law [7,11]:

$$TOL_i = \left(\frac{D_i C_S}{r_S}\right)^{1/2} \tag{5}$$

where D_i is the coefficient of oxygen diffusion in the considered principal direction of the composite material ($i = \perp$ or //), and C_S and r_S are the maximum values of the oxygen concentration and oxidation rate, respectively. Of course, these two last quantities are maximum on the rod surface.

By combining Equations (3) and (5), it becomes

$$\frac{TOL_{//}}{TOL_{\perp}} = \left(\frac{D_{//}}{D_{\perp}}\right)^{1/2} = \left(\frac{1 - V_f}{1 - \alpha\sqrt{V_f}}\right)^{1/2} \quad (6)$$

Thus, according to theory, the following should be found: $TOL_{//} = 1.9 \times TOL_{\perp}$ for a cubic stack. However, $TOL_{//}$ values reported in Table 3 are twice thicker at 210 °C and four times thicker at 180 °C than expected. This discrepancy can be only explained by the existence of a fiber/matrix interphase highly permeable to oxygen [12].

Anyway, in the radial direction, oxidation remains confined to the rod surface ($TOL_{\perp}$ corresponds to only 1–2% of the rod radius). It can be thus concluded that the micro-cavities induced by the thermolysis of the epoxy-anhydride matrix are the main damages altering the mechanical properties of the composite rod during its thermal ageing (see previous section).

3.3. Physicochemical Characterizations

Unfortunately, due not only to the high fraction of fibers (typically >60 vol%) in the composite rod but also to the initial presence of a very intense IR absorption band centered at 1735 cm^{-1} and assigned to ester groups (formed by the crosslinking reaction of the epoxy monomers with the anhydride hardener), it was very difficult to detect by FTIR spectrometry any chemical modification in the epoxy matrix during its thermal ageing between 180 and 210 °C. As an example, Figure 9 shows the IR spectra measured on the outer surface of the glass-fiber shell during the course of thermal ageing at 210 °C in ambient air.

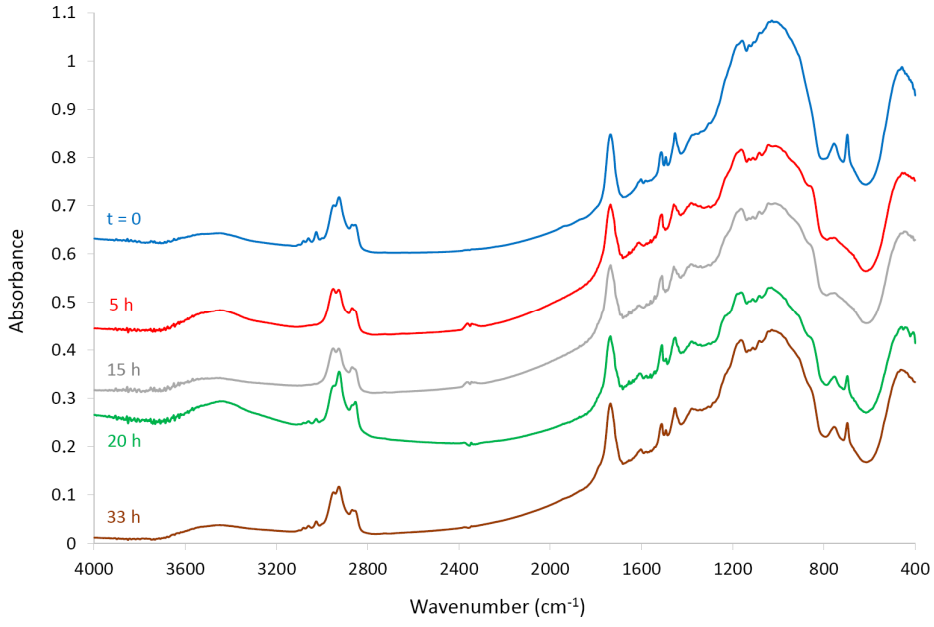

Figure 9. IR spectra of the outer surface of the glass-fiber shell before and after several durations of thermal ageing at 210 °C in ambient air.

The only chemical modifications that were detected by FTIR spectrometry for the epoxy-anhydride matrix occurred in the oxidized layer of the glass-fiber shell. As shown in Figure 10, a broadening of the base of the ester band was observed due to the appearance and accumulation of new carbonyl groups during the course of oxidation. The shoulder centered at 1785 cm^{-1} can be attributed to new

anhydride groups resulting from the condensation of carboxylic acids [13]. In contrast, the different shoulders centered at 1710, 1700, and 1690 cm^{-1} can be attributed to a large variety of other types of (saturated and unsaturated) carbonyl groups, for instance, aldehydes, carboxylic acids, and ketones. The formation of unsaturations is attested by the raising of the baseline between 1630 and 1670 cm^{-1}.

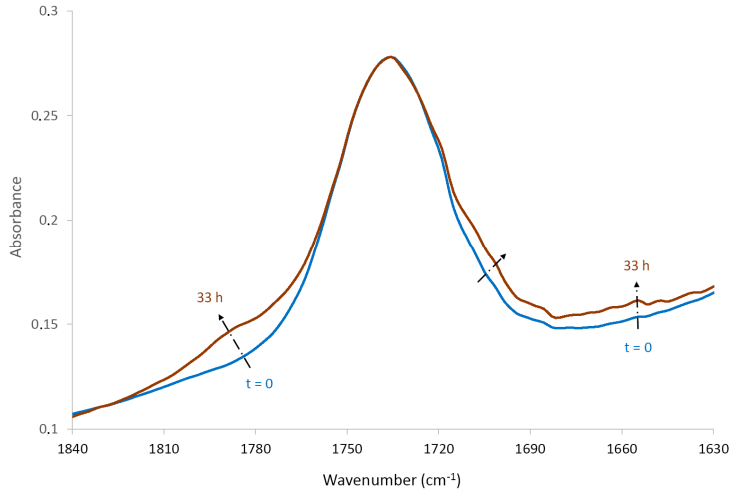

Figure 10. Modifications of the IR spectrum of the outer surface of the glass-fiber shell before and after 33 h of thermal ageing at 210 °C in ambient air.

In contrast, DSC was very useful to evidence the consequences of thermal degradation on the structure of the macromolecular network and, in particular, to reveal the inhibiting effect of oxygen on thermolysis. As an example, Figure 11 shows the changes in T_g at different depths in the rod diameter during the course of thermal ageing at 210 °C in ambient air.

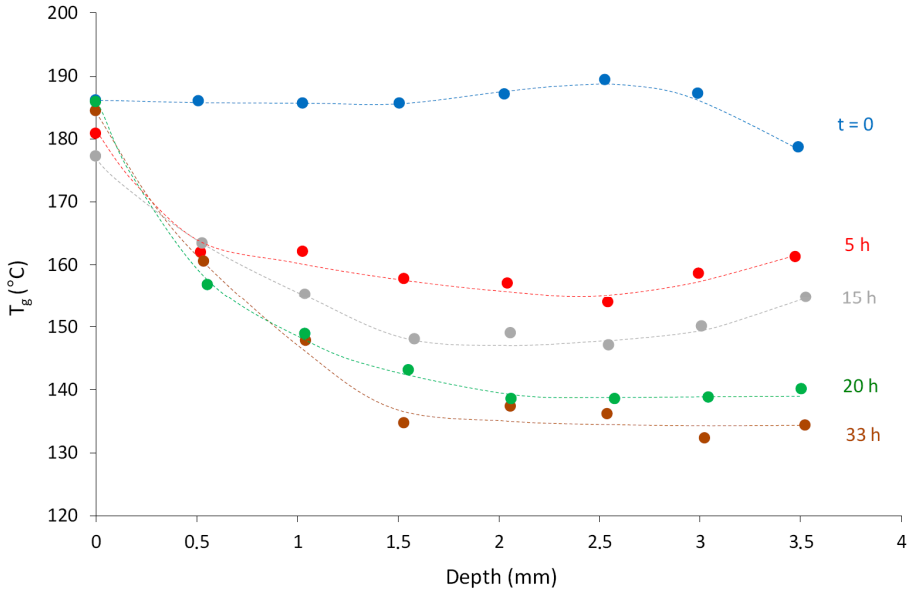

Figure 11. T_g profiles in the rod diameter before and after several durations of thermal ageing at 210 °C in ambient air.

These profiles call for the following comments:

- Between 180 and 210 °C, the thermolysis of the epoxy-anhydride matrix is far from being negligible. It consists of an efficient chain scission process leading to the destruction of elastically active chains and crosslink nodes and, thus, to a catastrophic decrease in T_g in the carbon-fiber core. The rate of

T_g decrease is maximum from the early periods of exposure and, then, slows down gradually so that T_g reaches an asymptotic value in the long term. The asymptotic values measured by DSC for the different ageing temperatures under study in the carbon-fiber core are reported in Table 4. All these values were confirmed by viscoelasticimetry.

- Thermolysis presumably consists of the thermal rearrangement of ester groups, a well-known reaction for linear polyesters [14–16]. Indeed, this reaction would lead to the formation of terminal carboxylic acids and double bonds. Then, the resulting carboxylic acids could condensate into anhydrides. All these chemical events are summarized in the mechanistic Scheme 1. They can explain the formation of a large part of the degradation products detected by FTIR spectrometry. It should be emphasized that the second chemical event (denoted T2 in Scheme 1) is assumed to generate volatile compounds such as cyclic anhydrides and water. It is in competition with the condensation of carboxylic acid chain ends, leading to the formation of new covalent bridges in the macromolecular network (see event T3 in Scheme 1).

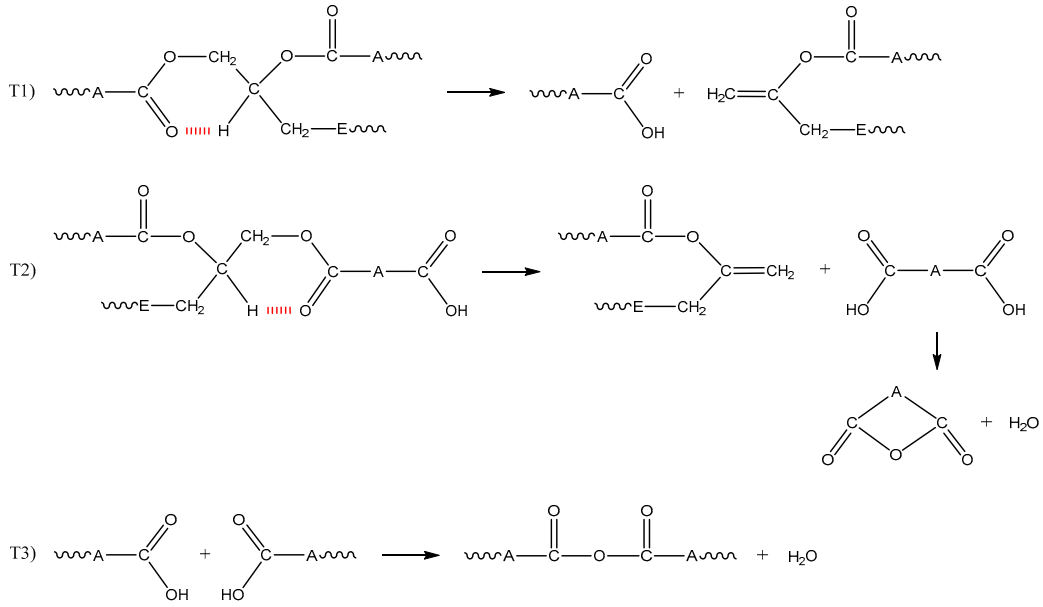

Scheme 1. General mechanistic scheme for the thermolysis of epoxy-anhydride matrices: Letters E and A designate epoxy monomer and anhydride hardener, respectively.

- In conclusion, thermolysis leads the formation and coalescence of many micro-cavities of gas in the carbon-fiber core (see Figure 7), thus inducing its catastrophic embrittlement (see Figure 4).

Table 4. Minimum values of T_g determined after long-term thermal ageing at 180 and 210 °C by DSC in the carbon-fiber core of the composite rod.

Ageing Conditions	T_g (°C)
Virgin rod	185.7 ± 3.1
300 h at 180 °C	142.3 ± 1.9
33 h at 210 °C	134.9 ± 1.9

- In addition, between 180 and 210 °C, the epoxy-anhydride matrix is very sensitive to oxidation because its chemical structure contains, as main reactive sites, very labile hydrogens located in the α position of a heteroatom (oxygen). Indeed, the corresponding C–H bonds are characterized by a much lower dissociation energy ($E_D \approx 376$ kJ·mol^{-1}) than in polyethylene ($E_D \approx 393$ kJ·mol^{-1}) [13,17,18]. Korcek et al. tried to correlate the rate constant k_3 for the

propagation of oxidation to the chemical structure of a series of hydrocarbon substrates. They found that Log(k_3) is a linear decreasing function of E_D of the weakest C–H bond [19].

- Since the oxidation kinetics is diffusion controlled, it leads to the formation of a superficial oxidized layer of which the maximal thickness in the radial direction is about 60 μm (see Table 3). In Figure 11, it can be clearly seen that oxidation inhibits almost totally thermolysis on the outer surface of the glass-fiber shell. This result is not surprising because the C–H bond involved in the thermolysis reaction (see Scheme 1) is also one of the two preferential oxidation sites in epoxy-anhydride matrices (denoted S2 in Scheme 2). It can be thus concluded that the radical attack on site S2 prevents the thermal rearrangement of the ester group, i.e., the thermolytic chain scission process.

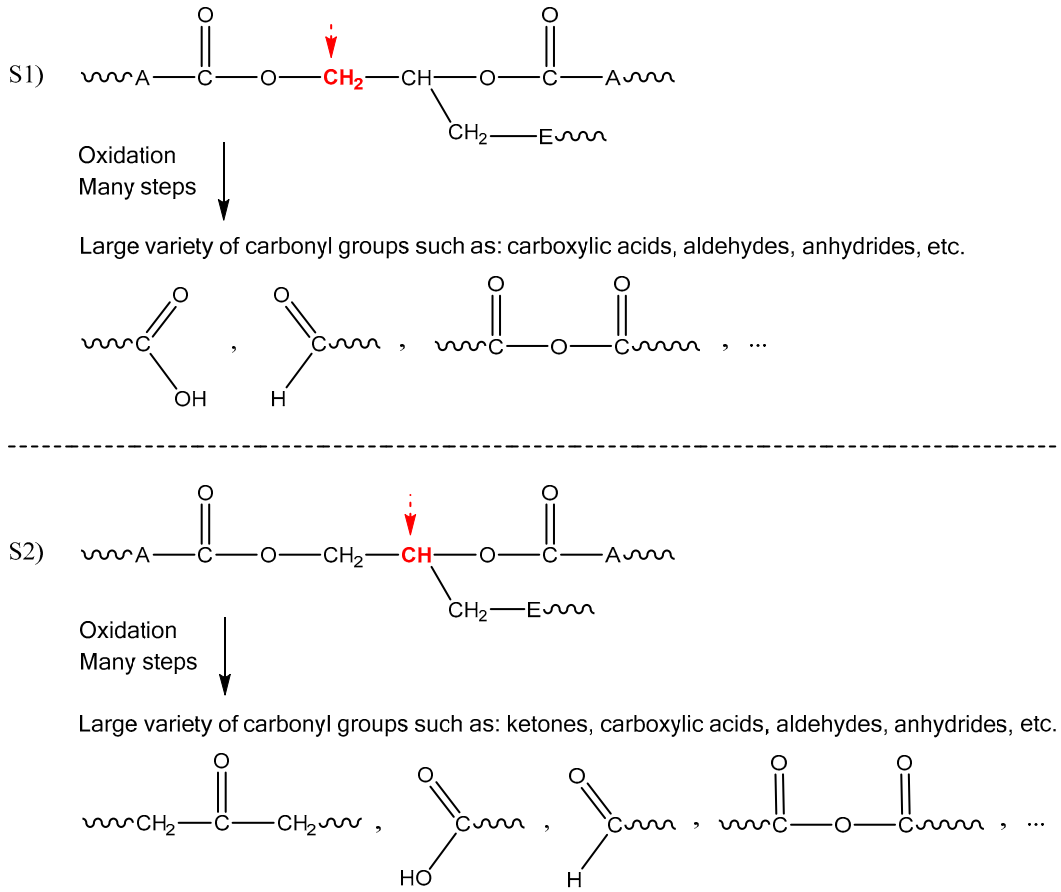

Scheme 2. Main reactive sites (denoted S1 and S2) in epoxy-anhydride matrices and their main carbonyl products.

- As shown in Figure 10, thermal oxidation leads to the formation of a large variety of new types of saturated and unsaturated carbonyl groups such as ketones, carboxylic acids, aldehydes, anhydrides, etc. The formation of saturated carbonyls can be easily explained by the radical attack on sites S1 and S2 (see Scheme 2). In contrast, the formation of unsaturated carbonyls is presumably due to the radical attack on a second population of sites (denoted S3 in Scheme 3): allylic hydrogens. Indeed, let us remember that allylic hydrogens are also very labile, certainly much more labile than hydrogens located in the α position of a heteroatom, given that the corresponding C–H bond is characterized by an even lower dissociation energy of only $E_D \approx 335$ kJ·mol^{-1} [20]. Thereafter, it will be considered that oxidation propagates almost instantaneously on site S3.
- It can be thus concluded that the mechanistic Schemes 1–3 allow explaining the formation of the vast majority of degradation products detected by FTIR spectrometry.

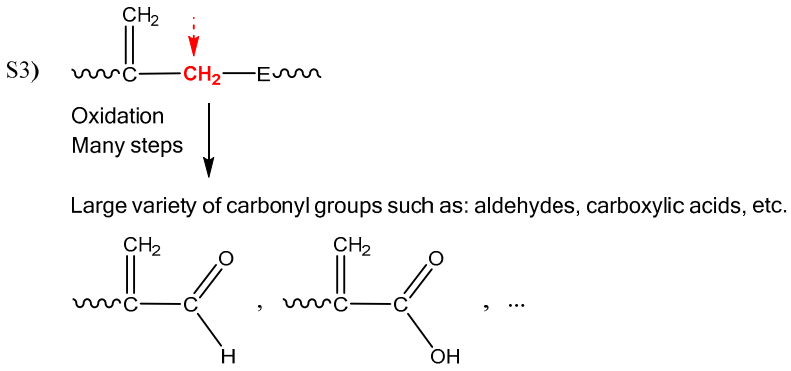

Scheme 3. New oxidation site (denoted S3) produced by thermolysis of the epoxy-anhydride matrices and its main carbonyl products.

Finally, thermogravimetry was very helpful for analyzing and elucidating the general trends of the thermal oxidation kinetics. Figure 12 shows some examples of mass changes in various nitrogen/oxygen gas mixtures between 180 and 210 °C of powder samples taken in the carbon-fiber core or glass-fiber shell.

(**a**)

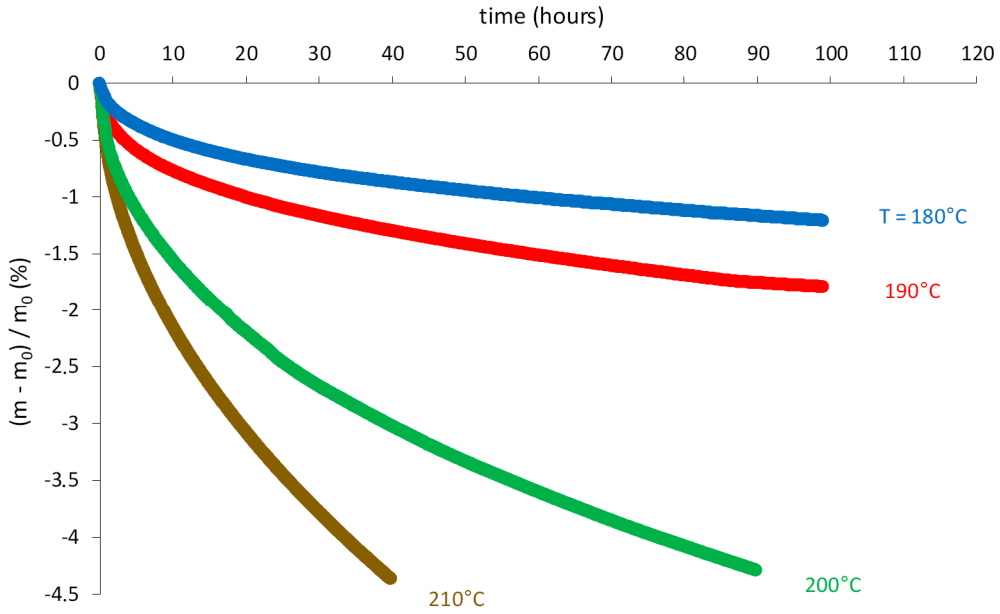

Figure 12. *Cont.*

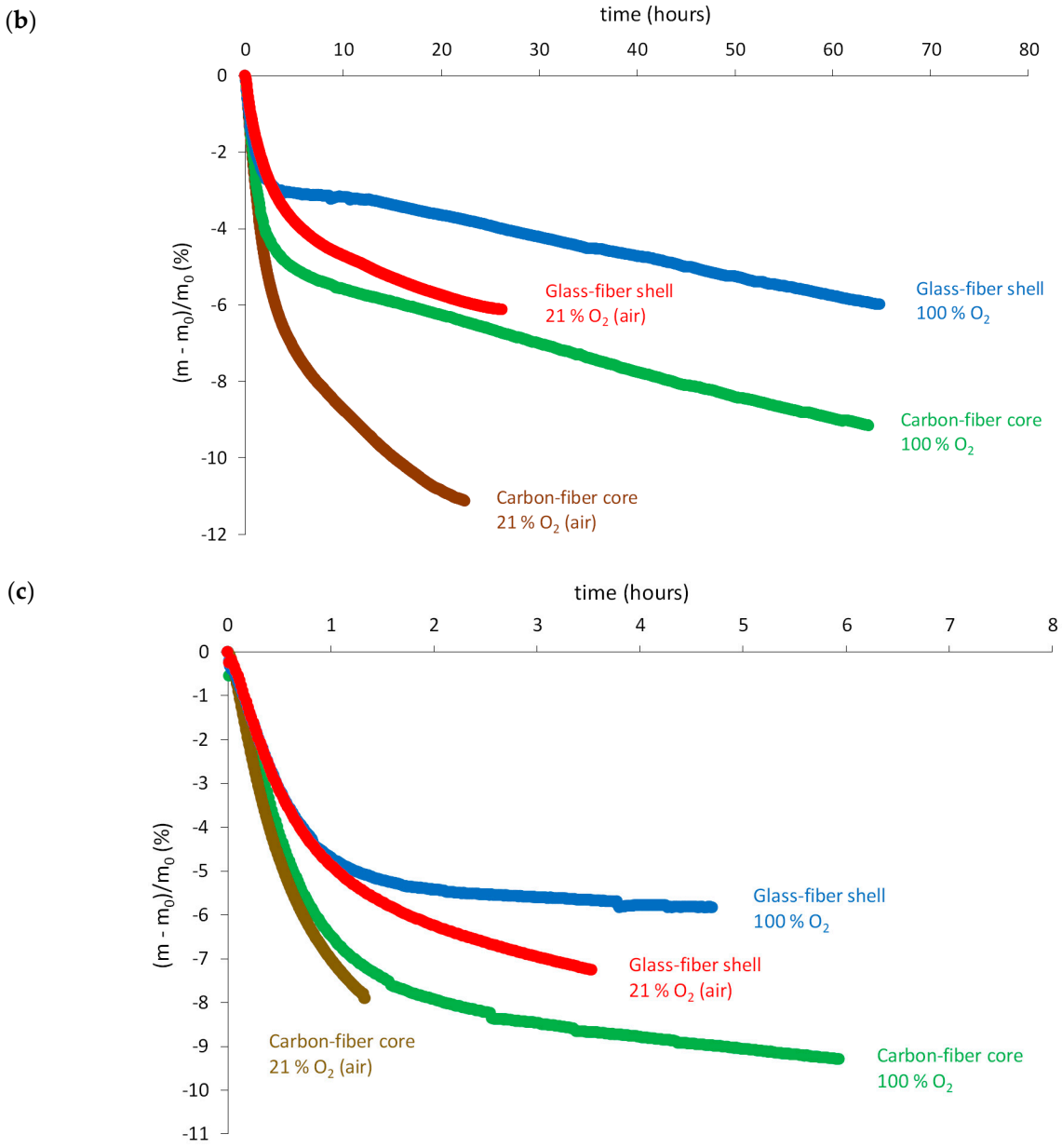

Figure 12. Mass changes of powder samples of carbon-fiber core in nitrogen between 180 and 210 °C (**a**), and carbon-fiber core and glass-fiber shell in air and pure oxygen at 180 °C (**b**) and 210 °C (**c**).

These kinetic curves call for the following comments:

- As expected, thermolysis leads to nonnegligible mass losses. As an example, the carbon-fiber core loses about −1% after a hundred hours in nitrogen at 180 °C and more than 4% after only a few dozen hours in nitrogen at 200 and 210 °C (Figure 12a). Thus, thermolysis is clearly thermo-activated.
- Thermal oxidation leads to stronger mass losses than thermolysis presumably because it produces a large amount of small molecules (mainly water and carbon dioxide), which can thus easily leave the epoxy-anhydride matrix. As an example, the carbon-fiber core loses more than 10% after only 15 h in air at 180 °C and after only a few hours in air at 210 °C (Figure 12b,c). Thus, thermal oxidation is also thermo-activated.
- Mass losses are much higher for the carbon-fiber core than for the glass-fiber shell presumably because of a large difference in the mass fraction of fibers. To check this assumption, let us note W_{mC} and W_{mV} as the respective mass fractions of epoxy-anhydride matrix in the two composite materials and the indexes C and V refer to carbon and glass fibers, respectively. If the same

mass loss of matrix occurred in both composite materials, then the following equality should be checked:

$$\left.\frac{\Delta m}{m_0}\right|_C = \frac{W_{mC}}{W_{mV}} \left.\frac{\Delta m}{m_0}\right|_V \quad (7)$$

W_{mC} and W_{mV} were directly determined in the cavity of the Netzsch Tg 209 thermogravimeter by heating the samples from 25 to 700 °C with a rate of 20 °C·min^{-1} under nitrogen until the complete pyrolysis of the epoxy-anhydride matrix. It was found that W_{mC} = 30 ± 3 wt% and W_{mV} = 16 ± 2 wt%, which allowed finally simplifying Equation (7) as follows:

$$\left.\frac{\Delta m}{m_0}\right|_C \approx 1.4 \times \left.\frac{\Delta m}{m_0}\right|_V \quad (8)$$

Figure 13 shows the same kinetic curves of mass changes of Figure 12b but is now readjusted to the same mass fraction of epoxy-anhydride matrix (i.e., 100 wt%) in both materials. It can be observed that the curves are superimposed almost perfectly, which validates Equation (7) and checks the initial assumption.

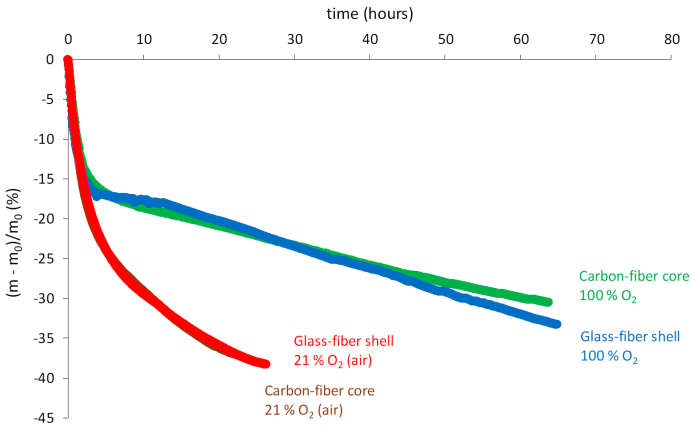

Figure 13. Mass changes of powder samples of carbon-fiber core and glass-fiber shell in air and pure oxygen at 180 °C but now readjusted to the same mass fraction of anhydride-epoxy matrix (i.e., 100 wt%) in both composite materials.

- In general, volatile compounds are formed in the initiation steps of oxidation. As an illustration, mechanistic Scheme 4 reports an example of a chemical event leading to the generation of two volatile compounds (water and carbon dioxide) during the unimolecular decomposition of hydroperoxides POOH, beforehand formed on sites S1 and S2. It should be specified that the rearrangement by β scission of alkoxy radicals PO$^{\bullet}$ occurs preferentially on the weakest bonds of the macromolecular skeleton, i.e., on the O–C bonds, which are characterized by a dissociation energy of only $E_D \approx 340$ kJ·mol^{-1} [20].

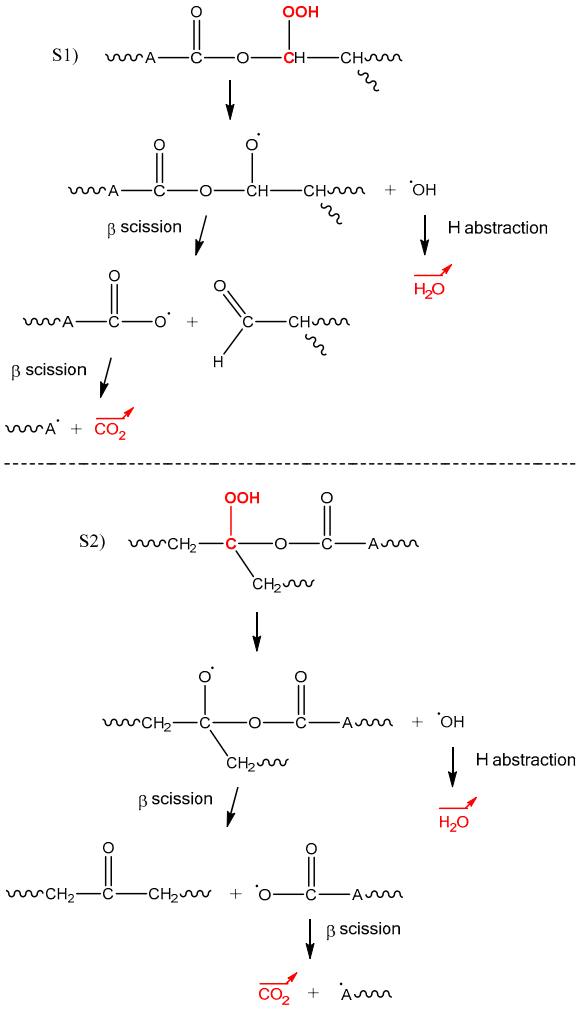

Scheme 4. Generation of volatile compounds (water and carbon dioxide) during the unimolecular decomposition of hydroperoxides.

- However, Figure 12b,c shows clearly that an increase of the oxygen partial pressure in the ageing environment (typically from 21% to 100% of the atmospheric pressure) leads to a significant reduction of mass losses. It can be thus concluded that an increase of the oxygen partial pressure favors more the incorporation of oxygen (i.e., mass gain) than the release of volatile compounds (i.e., mass loss). In Figure 12b, a slight hump of mass gain can even be observed between 10 and 20 h of exposure in pure oxygen at 180 °C. This peculiar behavior is presumably due to the existence of additional chemical events generating volatile fragments in oxygen default, which are however totally annihilated in oxygen excess. As an illustration, mechanistic Scheme 5 reports an example of a chemical event leading to the generation of one volatile fragment (carbon dioxide) during the rearrangement by β scission of alkyl radicals $P^{\bullet}$, beforehand formed on sites S1 and S2. As for alkoxy radicals $PO^{\bullet}$, this rearrangement occurs preferentially on the O–C bonds of the macromolecular skeleton. Of course, in the presence of oxygen, alkyl radicals $P^{\bullet}$ are quasi-instantaneously transformed into peroxy radicals $PO_2^{\bullet}$ propagating oxidation on sites S1 and S2, thus annihilating totally the formation of carbon dioxide.

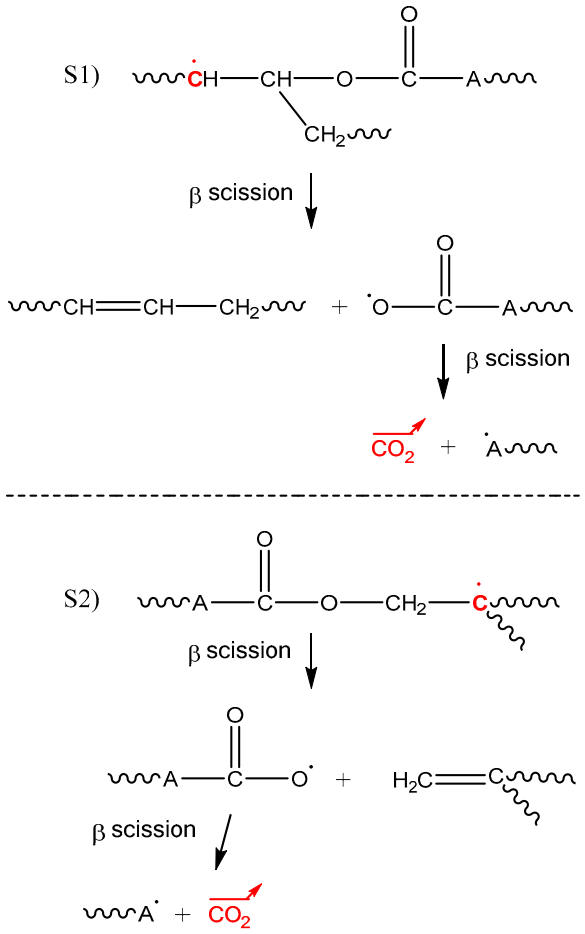

Scheme 5. Generation of volatile fragments (carbon dioxide) during the rearrangement of alkyl radicals.

4. Kinetic Modelling

A kinetic model was elaborated for simulating the kinetic curves of mass changes obtained in various nitrogen/oxygen gas mixtures between 180 and 210 °C on powder samples of carbon-fiber core and glass-fiber shell. This model is derived from a general mechanistic scheme taking into account all the different chemical events evidenced and discussed in previous sections.

4.1. Mechanistic Scheme

The mechanistic scheme is the combination of two distinct reactions. On one hand, thermolysis can be summarized by only two elemental steps:

$$0a) \quad Es \rightarrow (1 - \upsilon_0)Ac + F + \upsilon_0 V_0 \quad -PH \quad (k_{0a})$$

$$0b) \quad Ac + Ac \rightarrow An + H_2O \quad (k_{0b})$$

where Es, Ac, F, An and PH account for esters, carboxylic acids, unsaturations, anhydrides and oxidation sites, respectively. The first step brings together the two chemical events T1 and T2 previously detailed in Scheme 1. This step leads to the consumption of sites S2 and S1 and to the formation of allylic hydrogens as new reactive sites (of type S3; see Scheme 3) and are, thus, taken into account in the calculation of the global yield in reactive site PH. Finally, it produces small diacid molecules V_0 of molar mass M_{V0} with a yield υ_0. In contrast, the second step corresponds exactly to the last chemical event T3 of Scheme 1, producing water.

On the other hand, thermal oxidation is composed of at least ten elementary steps [17,18]: two initiations (1u and 1b), two propagations (2b and 3), and six bimolecular combinations between the different radical species (from 4 to 6d). In addition, it takes into account the rapid rearrangement by β scission of alkyl radicals $P^{\bullet}$ (denoted 2a):

$$1u) \quad POOH \rightarrow 2P^{\bullet} + H_2O + \upsilon_1 V_1 \quad -(2-\gamma_1)PH \quad (k_{1u})$$

$$1b) \quad 2POOH \rightarrow P^{\bullet} + PO_2{}^{\bullet} + H_2O + \upsilon_1 V_1 \quad -(1-\gamma_1)PH \quad (k_{1b})$$

$$2a) \quad P^{\bullet} \rightarrow P^{\bullet} + \upsilon_2 V_2 \quad -(1-\gamma_2)PH \quad (k_{2a})$$

$$2b) \quad P^{\bullet} + O_2 \rightarrow PO_2{}^{\bullet} \quad (k_{2b})$$

$$3) \quad PO_2{}^{\bullet} + PH \rightarrow POOH + P^{\bullet} \quad (k_3)$$

$$4) \quad P^{\bullet} + P^{\bullet} \rightarrow \gamma_4 P\text{-}P + (1-\gamma_4)PH + (1-\gamma_4)F + (1-\gamma_4)PH \quad (k_4)$$

$$5) \quad P^{\bullet} + PO_2{}^{\bullet} \rightarrow \gamma_5 POOP + (1-\gamma_5)POOH + (1-\gamma_5)F + (1-\gamma_5)PH \quad (k_5)$$

$$6a) \quad PO_2{}^{\bullet} + PO_2{}^{\bullet} \rightarrow [PO^{\bullet\bullet}OP]_{cage} + O_2 \quad (k_{6a})$$

$$6b) \quad [PO^{\bullet\bullet}OP]_{cage} \rightarrow POOP \quad (k_{6b})$$

$$6c) \quad [PO^{\bullet\bullet}OP]_{cage} \rightarrow An + Al \quad (k_{6c})$$

$$6d) \quad [PO^{\bullet\bullet}OP]_{cage} \rightarrow 2P^{\bullet} + 2\upsilon_1 V_1 \quad -2(1-\gamma_1)PH \quad (k_{6d})$$

where PH, POOH, $P^{\bullet}$, $PO_2{}^{\bullet}$, $PO^{\bullet}$, P-P, POOP, F, An, and Al account for reactive sites, hydroperoxides, alkyl, peroxy and alkoxy radicals, dialkyl and peroxide bridges, unsaturations, anhydrides, and alcohols, respectively. γ_1 is the yield in β scission of $PO^{\bullet}$ radicals (leading to aldehydes, ketones, and volatile fragments; see Scheme 4) in competition with hydrogen abstraction (leading to alcohols and carboxylic acids) in elementary steps 1u, 1b, and 6d. Similarly, γ_2 is the yield in β scission of $PO^{\bullet}$ radicals (leading to volatile fragments; see Scheme 5) in competition with hydrogen abstraction (leading to carboxylic acids) in elementary step 2a. In a first approach, each volatile fragment was assimilated to single average molecule V_i of molar mass M_{Vi} formed with a yield υ_i. Finally, γ_4 and γ_5 are the respective yields in coupling of alkyl-alkyl and alkyl-peroxy radicals in competition with disproportionation in termination steps 4 and 5. It should be specified that the different yields in reactive site PH take into account both the consumption of sites S1 and S2 and the formation of new reactive site S3.

4.2. System of Differential Equations

The following system of seven nonlinear differential equations (one equation per reactive species) was derived from the previous mechanistic scheme:

$$\frac{d[Es]}{dt} = -k_{0a} f_{PH} [Es] \tag{9}$$

$$\frac{d[Ac]}{dt} = (1-\upsilon_0) k_{0a} f_{PH} [Es] - 2k_{0b} [Ac]^2 \tag{10}$$

$$\frac{d[POOH]}{dt} = -k_{1u} f_{PH} [POOH] - 2k_{1b} f_{PH} [POOH]^2 + k_3 \left[PO_2^{\bullet}\right][PH] + (1-\gamma_5) k_5 \left[P^{\bullet}\right]\left[PO_2^{\bullet}\right] \tag{11}$$

$$\begin{aligned} \frac{d[P^{\bullet}]}{dt} = {} & 2k_{1u} f_{PH} [POOH] + k_{1b} f_{PH} [POOH]^2 - k_{2b} [P^{\bullet}][O_2] + k_3 \left[PO_2^{\bullet}\right][PH] - 2k_4 [P^{\bullet}]^2 \\ & - k_5 [P^{\bullet}]\left[PO_2^{\bullet}\right] + 2k_{6d} f_{PH} [PO^{\bullet\bullet}PO]_{cage} \end{aligned} \tag{12}$$

$$\frac{d\left[PO_2^{\bullet}\right]}{dt} = k_{1b} f_{PH} [POOH]^2 + k_{2b} \left[P^{\bullet}\right][O_2] - k_3 \left[PO_2^{\bullet}\right][PH] - k_5 \left[P^{\bullet}\right]\left[PO_2^{\bullet}\right] - 2k_{6a} \left[PO_2^{\bullet}\right]^2 \tag{13}$$

$$\frac{d[PO^{\bullet\bullet}PO]_{cage}}{dt} = k_{6a}\left[PO_2^{\bullet}\right]^2 - (k_{6b} + k_{6c} + k_{6d}f_{PH})\left[PO^{\bullet\bullet}PO\right]_{cage} \quad (14)$$

$$\begin{aligned}\frac{d[PH]}{dt} &= -k_{01}f_{PH}[Es] - (2-\gamma_1)k_{1u}f_{PH}[POOH] - (1-\gamma_1)k_{1b}f_{PH}[POOH]^2 - (1-\gamma_2)k_{2a}[P^{\bullet}] \\ &-k_3\left[PO_2^{\bullet}\right][PH] + (1-\gamma_5)k_5[P^{\bullet}]\left[PO_2^{\bullet}\right] + 2(1-\gamma_4)k_4[P^{\bullet}]^2 - 2(1-\gamma_1)k_{6d}f_{PH}[PO^{\bullet\bullet}PO]_{cage}\end{aligned} \quad (15)$$

where f_{PH} is a mathematical function introduced in the system of differential equations to avoid the substrate concentration $[PH]$ becoming negative at high conversion ratios of oxidation reaction. In a first approach, a hyperbolic mathematical form was chosen to describe the changes of f_{PH} with $[PH]$:

$$f_{PH} = \frac{[PH]}{[PH] + \varepsilon} \quad (16)$$

where typically $\varepsilon = 10^{-2} << 1$. This function does not introduce significant changes in the oxidation kinetics below a conversion value of about 99%.

The system of Equations (9)–(15) admits the following initial conditions (at $t = 0$):

- $[Es] = [Es]_0$
- $[Ac] = 0$
- $[POOH] = [POOH]_0$
- $[P^{\bullet}] = [PO_2^{\bullet}] = [PO^{\bullet\bullet}OP]_{cage} = 0$
- $[PH] = [PH]_0$

Typical values for epoxy-anhydride matrices are $[Es]_0 \approx 10$ mol·l^{-1} and $[PH]_0 \approx 24$ mol·l^{-1}.

At this stage, it is important to recall that $[POOH]_0$ does not correspond to the real initial concentration of hydroperoxides within the epoxy-anhydride matrix but often a higher value since it takes also into account the presence of "extrinsic" species, very difficult to titrate chemically (e.g., catalytic residues, polymer-oxygen complex, structural irregularities, etc.), which are also largely responsible for the earliest acts of oxidation. However, since the decomposition rate of these latter vanishes rapidly with time of exposure, POOH decomposition becomes rapidly the main source of radicals. If polymers are weakly pre-oxidized during the processing operations, $[POOH]_0$ is typically ranged between 10^{-5} and 10^{-1} mol·l^{-1} [21]. In a first approach, a value of $[POOH]_0 = 10^{-2}$ mol·l^{-1} was selected for this study.

In the case of thin films (of thickness lower than 100 μm) or powder samples, the oxygen concentration remains constant at any point of the sample volume throughout thermal ageing. Its value is given by the classical Henry's law:

$$[O_2] = [O_2]_0 = S \times P_{O2} \quad (17)$$

where S is the coefficient of oxygen solubility into the composite matrix and P_{O2} is the oxygen partial pressure in the ageing environment. Databases [22,23] show that S is almost independent of temperature for polymers. In a first approximation, the order of magnitude reported for S in aromatic epoxy-diamine matrices [18] was chosen for this study: $S = 1.6 \times 10^{-7}$ mol·l^{-1}·Pa^{-1}.

The system of Equations (9)–(15) was solved numerically using the semi-implicit algorithms recommended for stiff problems of chemical kinetics [24], in particular, the ODE23s solver of Matlab commercial software. Its resolution gave access to the changes with time of exposure of the main reactive species, i.e., [Es], [Ac], [POOH], $[P^{\bullet}]$, $[PO_2^{\bullet}]$, $[PO^{\bullet\bullet}OP]_{cage}$, and $[PH] = f(t)$. These quantities were then used to calculate the changes of important physicochemical properties easily measurable

experimentally to check the validity of the kinetic model, in particular, the rate of oxygen consumption and the release rate of the different volatile compounds:

$$\frac{d[O_2]_{abs}}{dt} = k_2\left[P^\bullet\right][O_2] - k_{6a}\left[PO_2^\bullet\right]^2 \tag{18}$$

$$\frac{d[V_0]}{dt} = v_0 k_{0a} f_{PH}[Es] \tag{19}$$

$$\frac{d[H_2O]}{dt} = k_{0b}[Ac]^2 + k_{1u} f_{PH}[POOH] + k_{1b} f_{PH}[POOH]^2 \tag{20}$$

$$\frac{d[V_1]}{dt} = v_1 k_{1u} f_{PH}[POOH] + v_1 k_{1b} f_{PH}[POOH]^2 + 2v_1 k_{6d} f_{PH}\left[PO^{\bullet\bullet}PO\right]_{cage} \tag{21}$$

$$\frac{d[V_2]}{dt} = v_2 k_{2a}\left[P^\bullet\right] \tag{22}$$

from which can be deduced the mass changes:

$$\frac{1}{m_0}\frac{dm}{dt} = W_m\left(\frac{32}{\rho}\frac{d[O_2]_{abs}}{dt} - \frac{M_{V0}}{\rho}\frac{d[V_0]}{dt} - \frac{18}{\rho}\frac{d[H_2O]}{dt} - \frac{M_{V1}}{\rho}\frac{d[V_1]}{dt} - \frac{M_{V2}}{\rho}\frac{d[V_2]}{dt}\right) \tag{23}$$

where ρ is the composite matrix density. A typical value for epoxy-anhydride matrices is $\rho \approx 1.27$ [25]. Introducing Equations (18)–(22) into Equation (23), it finally becomes the following:

$$\begin{array}{c}\frac{1}{m_0}\frac{dm}{dt} = \frac{W_m}{\rho}\left\{32\left(k_{2b}[P^\bullet][O_2] - k_{6a}\left[PO_2^\bullet\right]^2\right) - v_0 M_{V0} k_{0a} f_{PH}[Es] - 18k_{0b}[Ac]^2\right. \\ -(18 + v_1 M_{V1})\left(k_{1u} f_{PH}[POOH] + k_{1b} f_{PH}[POOH]^2\right) - v_2 M_{V2} k_{2a}[P^\bullet] \\ \left. -2v_1 M_{V1} k_{6d} f_{PH}[PO^{\bullet\bullet}PO]_{cage}\right\}\end{array} \tag{24}$$

4.3. Experimental Checking and Discussion

The kinetic model composed of Equations (9)–(24) was used as an inversed method to reproduce as well as possible the kinetic curves of mass changes shown in Figure 12 and to determine the values of the twenty one unknown parameters, i.e., the thirteen rate constants (from k_{0a} to k_{6d}), the five chemical yields (v_0, and from γ_1 to γ_5), and the three average molar masses (from v_0M_{V0} to v_2M_{V2}).

The first stage of the kinetic modelling consisted in the determination of the thermolysis parameters. In a first approach, it was assumed that the condensation of the terminal carboxylic acids is very difficult and, therefore, very slow. Thus, the corresponding rate constant k_{0b} was set to zero. Despite this restrictive hypothesis, Figure 14a shows a good agreement between theory and experiment. The values determined between 180 and 210 °C for the three remaining parameters (i.e., k_{0a}, v_0 and v_0M_{V0}) are given in Table 5.

Two distinct kinetic regimes are clearly observed. In rubbery state, k_{0a} increases rapidly with temperature, obeying an Arrhenius law with an activation energy of about 133 kJ·mol^{-1}. The value of k_{0a} previously reported in the literature for molten poly(ethylene terephthalate) (PET) at 280 °C [13] is found again by applying this law, which demonstrates the high heuristic value of the kinetic model. In contrast, in a glassy state, k_{0a} takes a very low value and seems to be independent of temperature. Similarly, in glassy state, parameters v_0 and v_0M_{V0} are much lower than in rubbery state, confirming that the thermolysis reaction occurs with difficulty because of the reduction of the molecular mobility.

The second stage of the kinetic modelling consisted in the determination of the thermal oxidation parameters while retaining the previous values for the thermolysis parameters. If agreed that the main oxidation sites are located in the α position of a heteroatom (sites S1 and S2 in Scheme 2), then these parameters should not significantly differ from the values recently reported in the literature for polyamides [17]. For this reason, the simulations started with the parameters already identified for polyamides but their values progressively changed if necessary. Figure 14b,c show a fairly good

agreement between theory and experiment. The values determined between 180 and 210 °C for the thermal oxidation parameters are also given in Table 5.

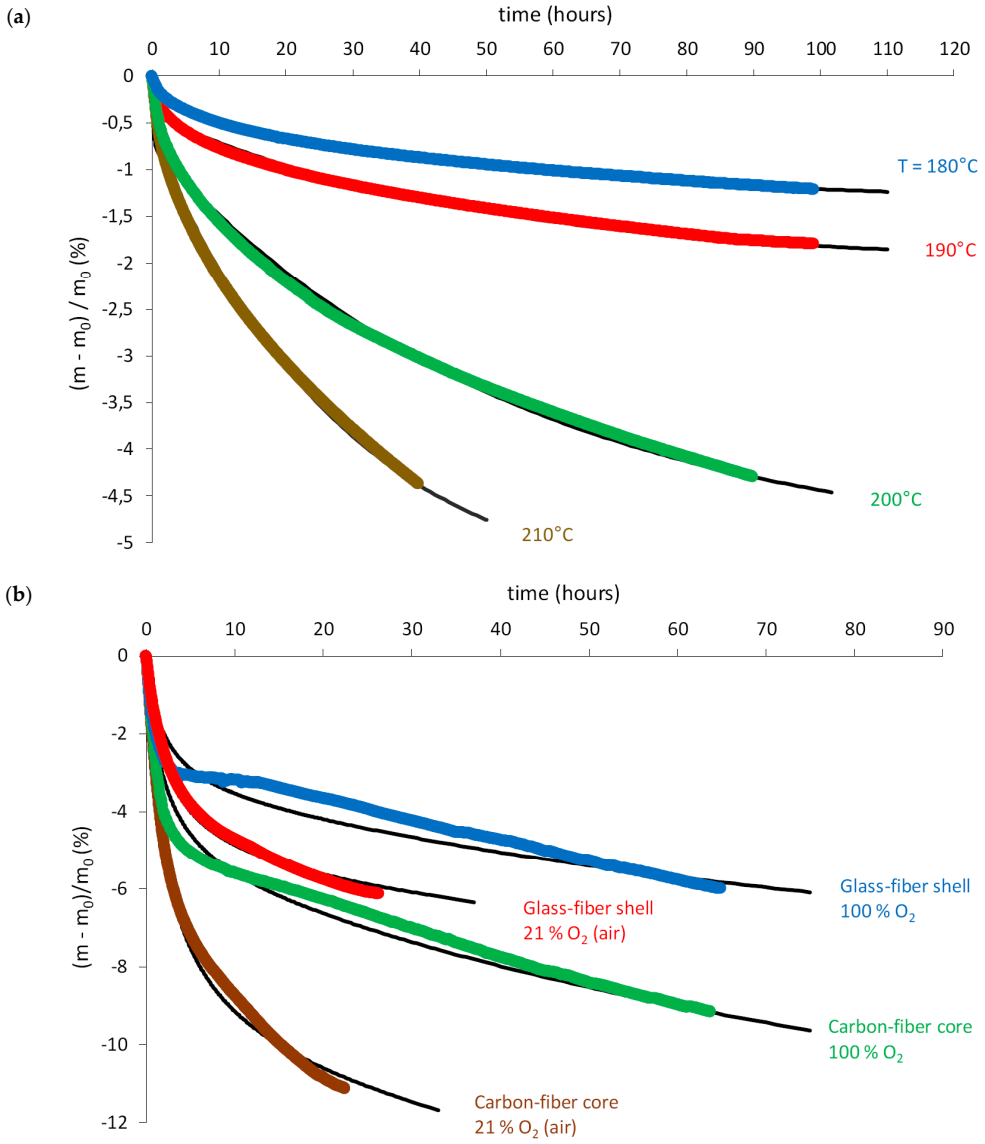

Figure 14. *Cont.*

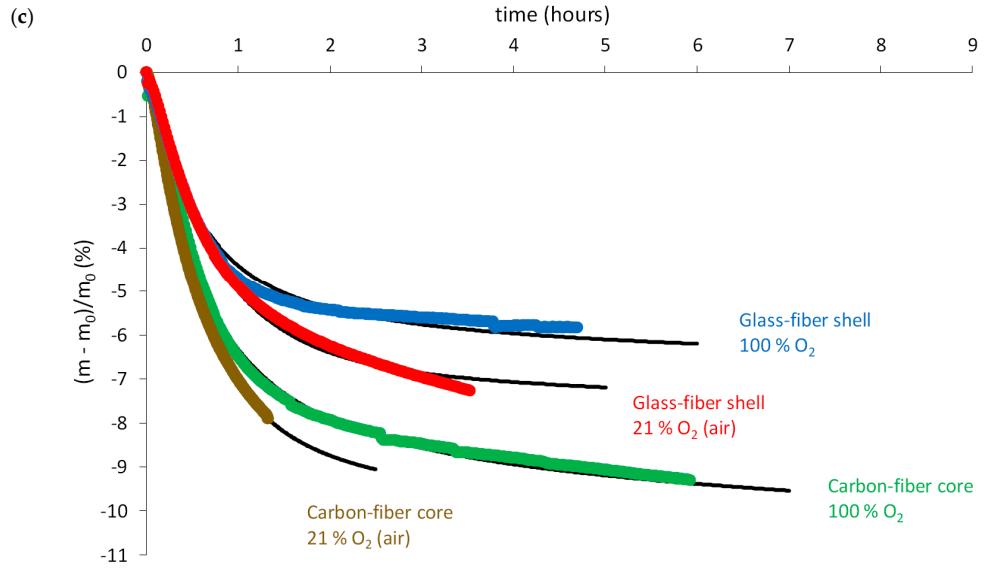

Figure 14. Mass changes of powder samples of carbon-fiber core in nitrogen between 180 and 210 °C (**a**) and of carbon-fiber core and glass-fiber shell in air and pure oxygen at 180 °C (**b**) and 210 °C (**c**): Comparison between simulations (black lines) and experimental data (color symbols).

Table 5. Parameters used for simulating the experimental data of Figure 14.

Parameter (unit)	Pre-Exponential Factor	Activation Energy ($kJ \cdot mol^{-1}$)	Comment	Reference
Rate constant				
k_{0a} (s^{-1})	5.8×10^{-6}	0	$T \leq 190$ °C	This study
	2.5×10^{9}	133	$T \geq 200$ °C	
k_{0b} ($l \cdot mol^{-1} \cdot s^{-1}$)	0	–	–	This study
k_{1u} (s^{-1})	7.6×10^{12}	132	–	[17]
k_{1b} ($l \cdot mol^{-1} \cdot s^{-1}$)	1.4×10^{9}	94	–	[17]
k_{2a} (s^{-1})	2.4×10^{5}	0	–	This study
k_{2b} ($l \cdot mol^{-1} \cdot s^{-1}$)	10^{8}	0	–	[17]
k_{3} ($l \cdot mol^{-1} \cdot s^{-1}$)	1.8×10^{9}	63	–	[17]
k_{4} ($l \cdot mol^{-1} \cdot s^{-1}$)	8×10^{11}	0	–	[17]
k_{5} ($l \cdot mol^{-1} \cdot s^{-1}$)	4×10^{11}	0	–	This study
k_{6a} ($l \cdot mol^{-1} \cdot s^{-1}$)	8.4×10^{16}	63	–	This study
k_{6b} (s^{-1})	9×10^{7}	0	–	This study
k_{6c} (s^{-1})	9×10^{7}	0	–	This study
k_{6d} (s^{-1})	4.1×10^{12}	43	–	This study
Chemical yield				
υ_0 (%)	6 ± 1	–	$T \leq 190$ °C	This study
	20 ± 2	–	$T \geq 200$ °C	
γ_1 (%)	90	–	–	This study
γ_2 (%)	70	–	$T \leq 190$ °C	This study
	10	–	$T \geq 200$ °C	
γ_4 (%)	45 ± 5	–	$T \leq 190$ °C	This study
	10	–	$T \geq 200$ °C	
γ_5 (%)	45 ± 5	–	$T \leq 190$ °C	This study
	10	–	$T \geq 200$ °C	
Molar mass				
$\upsilon_0 M_{V0}$ ($g \cdot mol^{-1}$)	5.5 ± 1.3	–	$T \leq 190$ °C	This study
	20 ± 1.7	–	$T \geq 200$ °C	
$\upsilon_1 M_{V1}$ ($g \cdot mol^{-1}$)	48	–	–	This study
$\upsilon_2 M_{V2}$ ($g \cdot mol^{-1}$)	11	–	–	This study

They call for the following comments:

- Half of the constant rates of the thermal oxidation reaction (from k_{1u} to k_4) took the same values as in polyamides [17]. All others (from k_5 to k_{6d}) took very close values, thus confirming the initial assumption. The main difference between the oxidative behaviors of epoxy-anhydride matrices and PET is the presence of an additional radical rearrangement. To our knowledge, the value of the corresponding rate constant k_{2a} has never been reported in the literature. The fact that k_{2a} takes a very high value and is independent of temperature clearly indicates the high instability of the alkyl radicals $P^{\bullet}$ involved in the corresponding reaction.
- As for thermolysis, a change in kinetic regime is detected near T_g for thermal oxidation, but only some chemical yields (from γ_2 to γ_5) are affected. It can thus be concluded that the impact of molecular mobility on the thermal oxidation kinetics is much more reduced than on the thermolysis kinetics.
- Finally, a value higher than the molar mass of carbon dioxide (i.e., 44 g·mol^{-1}) was found for $\upsilon_1 M_{V1}$, thus suggesting that volatile fragments heavier than carbon dioxide are also formed during the rearrangement by β scission of alkoxy radicals $PO^{\bullet}$. A more detailed knowledge of the chemical structure of the epoxy-anhydride matrix would be necessary to identify these volatile fragments and to propose a possible mechanistic scheme for their formation.

4.4. Towards a Nonempirical Prediction of Damage Development

Prior to mass changes, the kinetic model gives access to the concentrations of several small molecules produced by the thermal ageing (see Equations (19)–(22)). In the case of thin films (of thickness lower than 100 μm) or powder samples, these molecules evaporate almost instantaneously. They are thus rightly qualified "volatile products", and Equations (19)–(22) can be used to calculate their corresponding concentration. However, in the case of the hybrid composite rod, these molecules first have to migrate (by diffusion) up to the outer surface of the glass-fiber shell to be released. Depending on their diffusivity, a large quantity of these molecules will remain trapped in the carbon-fiber core, where they will accumulate. In this case, the Fick's second law needs to be introduced in Equations (19)–(22) to calculate their local concentration in the carbon-fiber core.

Some of these molecules (such as diacid fragments and water) are very polar and, thus, are characterized by a very high value of solubility parameter (e.g., δ = 48 MPa$^{1/2}$ for water), whereas epoxy-anhydride matrices are known to be moderately polar polymers (δ = 22.7 MPa$^{1/2}$) [26]. For this reason, these molecules are also characterized by a low solubility threshold in epoxy-anhydride matrices. When their concentration will exceed this critical value, a phase separation is expected to occur in the composite matrix, leading to the formation of micro-cavities of gaz. Such a scenario was evidenced in a very different situation: the radiochemical ageing of poly(methyl methacrylate) (PMMA) [27].

At this stage of investigations, the kinetic model cannot be used to calculate the initiation and development of damage in the carbon-fiber core due to the ignorance of the solubility thresholds of diacid fragments and water. These quantities can be obtained from sorption experiments in acidic solutions and distilled water, respectively.

5. Conclusions

Analytical investigations (with FTIR spectrometry, thermogravimetry, differential calorimetry, optical microscopy, and three-point bending) have clearly shown the low thermal stability of the hybrid composite rod at high temperature. Between 180 and 210 °C, the thermolysis of the epoxy-anhydride matrix induces significant damage in the carbon-fiber core (chain scissions, formation of gases, mass losses, initiation, and coalescence of micro-cavities), thus altering catastrophically the mechanical properties of the composite rod. In contrast, thermal oxidation inhibits thermolysis in a too thin superficial layer (typically 60 μm) of the glass-fiber shell to have a decisive impact.

Since thermolysis is characterized by a high activation energy (typically about 204 kJ·mol^{-1}, against about 130 kJ·mol^{-1} for thermal oxidation), it cannot be excluded that this composite material satisfies finally the industrial requirements to be used for the reinforcement of next generation overhead power lines in the current operating conditions, i.e., typically between 70 and 90 °C.

Additional experiments need to be performed at temperatures lower than 18 °C to answer this question. Moreover, the kinetic model needs to be completed to predict not only the concentrations of volatile compounds and the resulting mass changes but also the initiation and development of damage in the carbon-fiber core. Finally, a critical size of damage needs to be proposed as end-of-life criterion and, then, introduced into the kinetic model to predict the lifetime of the composite rod. All these research works will be the subject of future publications.

Author Contributions: G.M. performed the experiments; G.M. and X.C. analyzed the data; X.C. developed the kinetic model and performed the simulations; X.C. wrote the paper.

Funding: This research was funded by the EDF Research Center Les Renardières, Ecuelles, France.

Conflicts of Interest: The authors declare no conflict of interest.

References

1. Dal Maso, F.; Mézière, J. Calcul des propriétés élastiques des tissus utilisés dans les matériaux composites. *Rev. IFP* **1998**, *53*, 857–870. [CrossRef]
2. Belluci, F. Galvanic corrosion between non-metallic composites and metals. II: Effects of area ratio and environmental degradation. *Corrosion* **1992**, *48*, 281–291. [CrossRef]
3. Barjasteh, E.; Bosje, E.J.; Tsai, Y.I.; Nutt, S.R. Thermal ageing of fiberglass/carbon-fiber hybrid composites. *Composites A* **2009**, *40*, 2038–2045. [CrossRef]
4. Tsai, Y.I.; Bosze, E.J.; Barjasteh, E.; Nutt, S.R. Influence of hygrothermal environement on thermal and mechanical properties of carbon fiber/fiberglass hybrid composites. *Compos. Sci. Technol.* **2009**, *69*, 432–437. [CrossRef]
5. Barjasteh, E.; Kar, N.; Nutt, S.R. Effect of filler on thermal aging of composites for next-generation power lines. *Composites A* **2011**, *42*, 1873–1882. [CrossRef]
6. NF EN ISO 178. *Plastiques—Détermination des Propriétés en Flexion*; AFNOR Editions: La Plaine Saint-Denis, France, 2011.
7. Colin, X.; Mavel, A.; Marais, C.; Verdu, J. Interaction between cracking and oxidation in organic matrix composites. *J. Compos. Mater.* **2005**, *39*, 1371–1389. [CrossRef]
8. Kondo, K.; Taki, T. Moisture diffusivity of unidirectional composites. *J. Compos. Mater.* **1982**, *16*, 82–93. [CrossRef]
9. Whitcomb, J.; Xiaodong, T. Micromechanics of moisture diffusion in composites with impermeable fibers. *J. Compos. Mater.* **2002**, *36*, 1093–1101. [CrossRef]
10. Tsai, S.W. *Composite Design*, 4th ed.; Think Composites: Dayton, OH, USA, 1988.
11. Audouin, L.; Langlois, V.; Verdu, J.; De Bruijn, J.C.M. Role of oxygen diffusion in polymer ageing: Kinetic and mechanical aspects. *J. Mater. Sci.* **1994**, *29*, 569–583. [CrossRef]
12. Defauchy, V.; Le Corre, H.; Colin, X. Simulation of the oxygen permeability of a composite container. *J. Compos. Sci.* **2018**, *2*, 21. [CrossRef]
13. Nait-Ali, L.K.; Colin, X.; Bergeret, A. Kinetic analysis and modeling of PET macromolecular changes during its mechanical recycling by extrusion. *Polym. Degrad. Stab.* **2011**, *96*, 236–246. [CrossRef]
14. Passalacqua, V.; Pilati, F.; Zamboni, V.; Fortunato, B.; Manaresi, P. Thermal degradation of poly(butylene terephthalate). *Polymer* **1976**, *17*, 1044–1048. [CrossRef]
15. Assadi, R.; Colin, X.; Verdu, J. Irreversible structural changes during PET recycling by extrusion. *Polymer* **2004**, *45*, 4403–4412. [CrossRef]
16. Lopez Arraiza, A.; Sarasua, J.R.; Verdu, J.; Colin, X. Rheological behavior and modelling of thermal degradation of poly(ε-caprolactone) and poly(l-lactide). *Int. Polym. Process.* **2007**, *22*, 389–394. [CrossRef]
17. El Mazry, C.; Ben Hassine, M.; Correc, O.; Colin, X. Thermal oxidation kinetics of free additive polyamide 6-6. *Polym. Degrad. Stab.* **2013**, *98*, 22–36. [CrossRef]

18. Colin, X.; Fayolle, B.; Cinquin, J. Nouvelles avancées en modélisation cinétique de la thermo-oxydation des matrices époxy-diamines. *Matériaux Tech.* **2016**, *104*, 202. [CrossRef]
19. Korcek, S.; Chenier, J.H.B.; Howard, J.A.; Ingold, K.U. Absolute rate constants for hydrocarbon autoxidation. XXI. Activation energies for propagation and the correlation of propagation arte constants with carbon-hydrogen bond strengths. *Can. J. Chem.* **1972**, *50*, 2285–2297. [CrossRef]
20. Colin, X.; Teyssèdre, G.; Fois, M. Ageing and degradation of multiphase polymer systems. In *Handbook of Multiphase Polymer Systems*; Boudenne, A., Ibos, L., Candau, Y., Thomas, S., Eds.; John Wiley & Sons Ltd.: Chichester, UK, 2011; Volume 2/2, Chapter 21, pp. 797–841. ISBN 978-0-4707-1420-1.
21. Colin, X.; Fayolle, B.; Audouin, L.; Verdu, J. About a quasi-universal character of unstabilised polyethylene thermal oxidation kinetics. *Polym. Degrad. Stab.* **2003**, *80*, 67–74. [CrossRef]
22. Van Krevelen, D.W.; Te Nijenhuis, K. *Properties of Polymers. Their Correlation with Chemical Structure. Their Numerical Estimation and Prediction from Additive Group Contributions*, 4th ed.; Elsevier: Amsterdam, The Netherlands, 2009; Chapter 18, pp. 655–702. ISBN 978-0-08-054819-7.
23. Stannet, V. Simples gases. In *Diffusion in Polymers*; Crank, J., Park, G.S., Eds.; Academic Press Inc.: London, UK, 1968; Chapter 2, pp. 41–73. ISBN 0-12-197050-7.
24. Hairer, E.; Wanner, G. *Solving Ordinary Differential Equations II. STIFF and Differential Algebraic Problems*; Springer: Berlin, Germany, 1991; Chapter IV, pp. 1–239. ISBN 978-3-540-60452-5.
25. Pascault, J.-P.; Sautereau, H.; Verdu, J.; Williams, R.J.J. *Thermosetting Polymers*; Marcel Dekker, Inc.: New York, NY, USA, 2002; Chapter 10, pp. 282–322. ISBN 0-8247-0670-6.
26. Colin, X. Nonempirical kinetic modelling of non-Fickian water absorption induced by a chemical reaction in epoxy-amine networks. In *Durability of Composites in a Marine Environment 2, Solid Mechanics and Its Applications 245*; Davies, P., Rajapakse, Y.D.S., Eds.; Springer: Dordrecht, The Netherlands, 2018; Chapter 1, pp. 1–18. ISBN 978-3-319-65144-6.
27. Bovey, F.A. *Effect of Ionizing Radiation on Synthetic and Natural Polymers*; Interscience Publishers, Inc.: New York, NY, USA, 1958.